Supplementary Materials

Feasibility Study of Single-crystal Si Islands Manufacturing by Microscale Printing of Nanoparticles and Laser Crystallization

Wan Shou, [†,1] Brandon Ludwig,[†,1] Letian Wang,[‡] Xiangtao Gong, [†] Xiaowei Yu, [†] Costas Grigoropoulos,[‡] Heng Pan[,†]*

Affiliations

[†]Department of Mechanical and Aerospace Engineering, Missouri University of Science and Technology, Rolla, 65409, USA

[‡]Laser Thermal Laboratory, Department of Mechanical Engineering, University of California, Berkeley, California, 94720-1740, USA

*Corresponding author: HP. Email hp5c7@mst.edu

Si nanopowder

Silicon nanoparticles (type C, ACS Material LLC) are used in this study. The representative TEM image and XRD of these particles are shown below (the image and XRD are from https://www.acsmaterial.com/media/catalog/product/t/d/tds-silicon_nanoparticles.pdf). The particles show typical crystallinity of Si powders and have averaged size ~30-50nm.

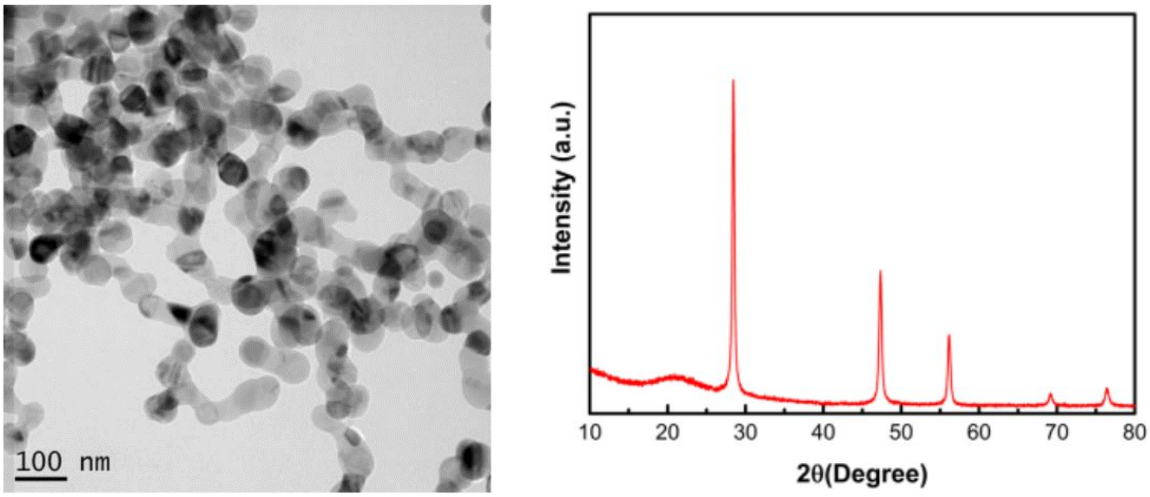

Fig. S1. TEM and XRD of Si nanoparticles.

Aerosol printing

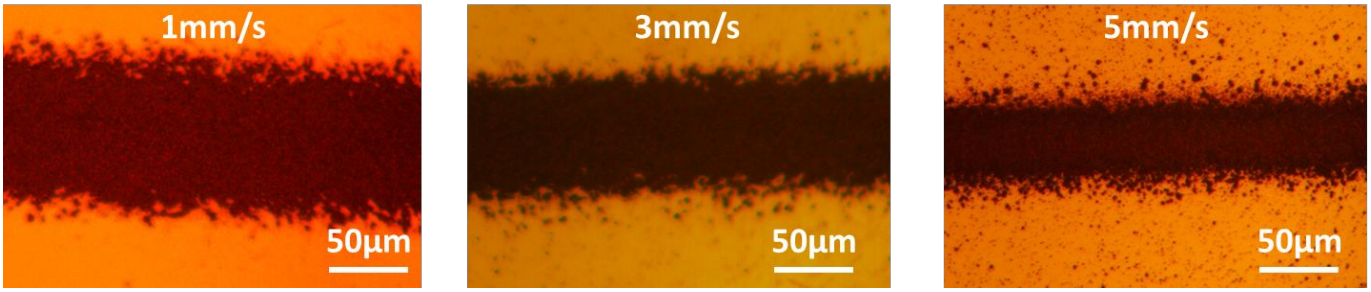

Fig. S2. The influence of printing speed on printed linewidth.

A home-built aerosol printer was used for Si ink printing. Aerosol printing was completed using pneumatic nebulizers to aerosolize the Si ink. The aerosol was focused by nozzle for direct printing of ribbons. The linewidth generally decreases with the increase of printing speed, in the range of 20-100 μm. The smallest continuous line printed in our study was about 20 μm. For the crystallization, lines of 40-50 μm were used to ensure sufficient materials and smaller than the laser spot (~80 μm).

Confined crystallization system

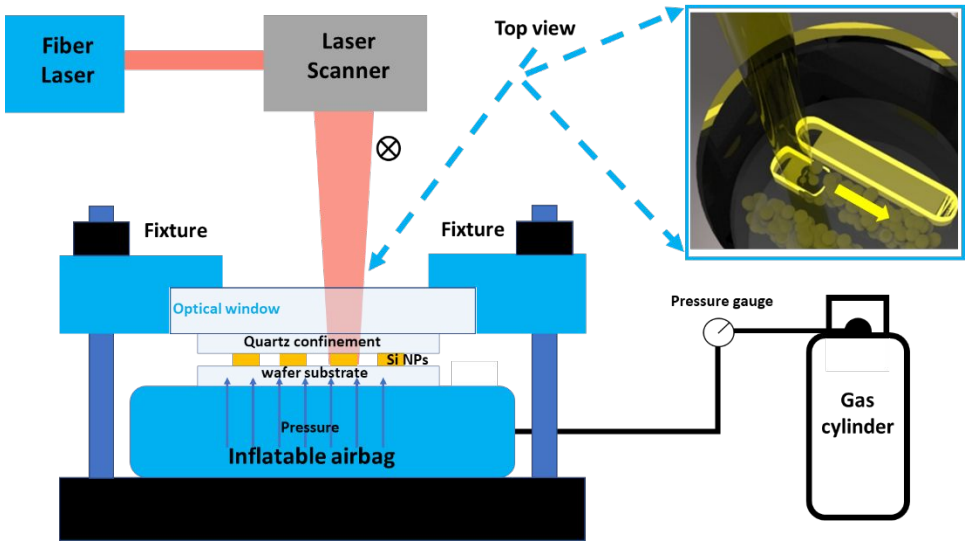

Fig. S3. Schematics of confined laser processing setup. (Inset shows the laser moving direction, along the printed Si line)

In order to realize confined crystallization, a confined laser processing setup was developed as shown in Fig. S3. An IPG Fiber Laser (1065 nm, CW, 100 W) was directed into a galvanometer (laser scanner) for high speed laser sintering and crystallization. This laser was chosen because it economically delivers sufficiently high laser power that can be absorbed by silicon, which is an indirect bandgap semiconductor. Since lasers with higher photon energy, such as green laser, would cost more to deliver similar level of power, this laser at near-IR wavelength was chosen. A defocused laser spot with diameter of ~80 μm was selected to cover the whole printed Si line. A broadband precision window (provided by ThorLabs) was used as the optical window, allowing the laser pass through and directly contacting the quartz confinement. The optical window was assembled with a mechanical fixture system, which fixs the up side of the processing setup. A fused quartz slide was purchased from Ted Pella, which is made from high purity fused quartz (with a nominal softening point of 1683˚C), was used as the confinement. Silicon wafer with 2 μm thermal oxide was provided by University Wafer and used as the substrate. A customized inflatable airbag was bought from MatJack Inc. to planarize the Si nanoparticles with uniform pressure (up to 120 psi). The assembling sequence from bottom to up is airbag, wafer substrate (with Si NPs line on it), quartz confinement, and optical window. By inflating the airbag through a gas cylinder, where a pressure gauge was used to monitor the pressure, pressure can be applied from the bottom of the wafer to planarized the Si NPs. The applied pressure can be adjusted up 120 psi, typically, 100, 110, 115, and 120 psi were used for sintering. The laser scanned along the line as shown in the inset of Fig. S3.

Workflow

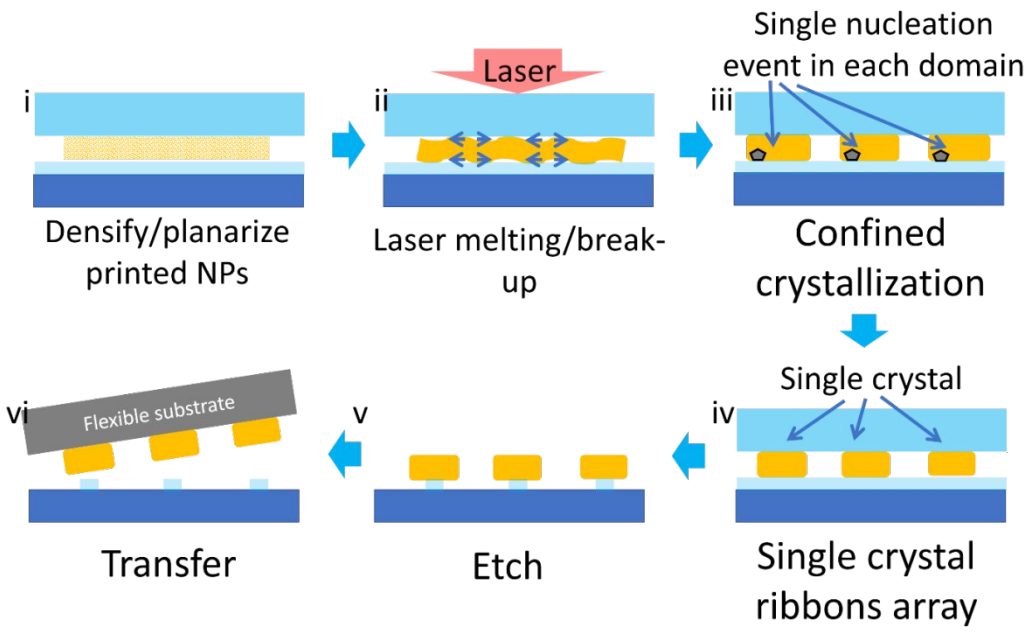

Fig. S4. The workflow of confined laser melting, crystallization and transfer printing.

The processing of single-crystal fabrication can be separated into two parts (Fig. S4): the first part is confined laser melting and crystallization (i-iv); the second part is the transfer printing (v and vi).

Substrate effects on ribbon morphology

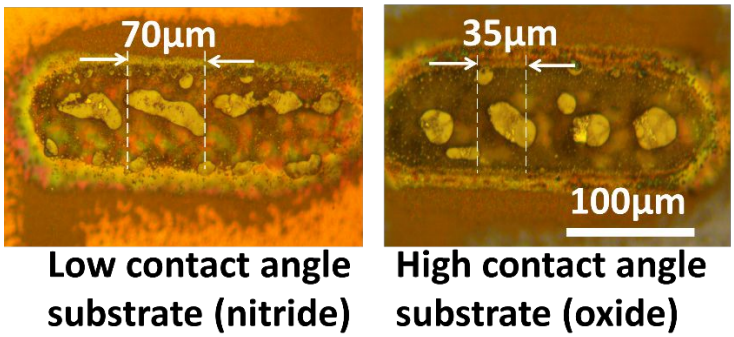

Fig. S5. Ribbon morphology on different substrates.

Due to the low contact angle between molten Si and nitride, molten Si is easier to spread out on nitride substrate compared with on oxide substrate. As shown in Fig. S5, Si islands can be as long as ~70μm on silicon nitride substrate while they are around 35μm on silicon oxide substrate.

Computational Fluid Dynamics simulation

A Finite Difference Method (FDM) numerical computation of the full Navier-Stokes equation based on the volume-of-fluid (VoF) interface tracking method is used to simulate the evaluation of liquid ribbon break-up process. This method has been recently applied to reproduce the Rayleigh-Plateau instability for nano- and microscale liquid filaments [Hartnett2015; Ubal2014]. Wall-adhesion model is invoked to model contact angles. Navior's slip condition has been included. The commercial software FLUENT is employed to perform the simulation.

To consider the particle packing, the initial particle configuration is obtained from a separate Discrete Element Modeling (DEM) where NP packing have been simulated (as shown in Fig. S6). With this model, the instability as a function of powder density can be studied. In the 2D simulation, nanoparticles with diameter ~500 nm were packed to different packing density as controlled by the gap distance. In the simulation, the nanoparticles were set to be melted (liquid) at t=0s. Simulations (Fig. S6-b) show that with 62.5% powder packing density, the film breaks up into several segments within a few μs with contact angle 80º (<90º). By increasing packing density to 74.5%, break-up is largely suppressed as shown by continuous stripe after a few μs. The simulation indicates the break-up can be suppressed or delayed by increasing powder packing density.

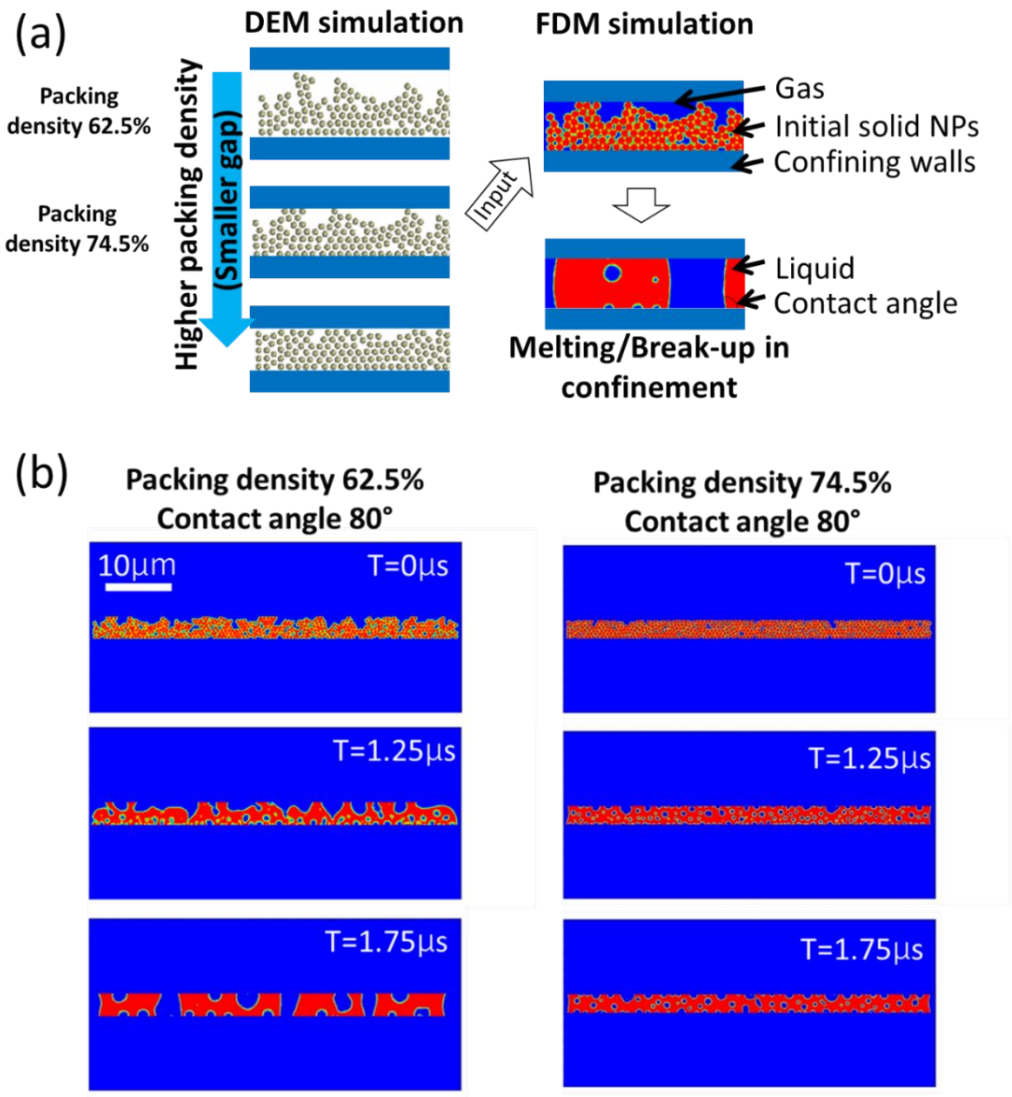

Fig. S6. Simulation scheme to study break-up of melted nanoparticles in confined configuration. (a) DEM simulation and FDM simulation of nanoparticle packing and melting/break-up in confinement (b) Break-up processes of melted nanoparticles at different packing density.

Energy-dispersive X-ray (EDX) spectroscopy characterization

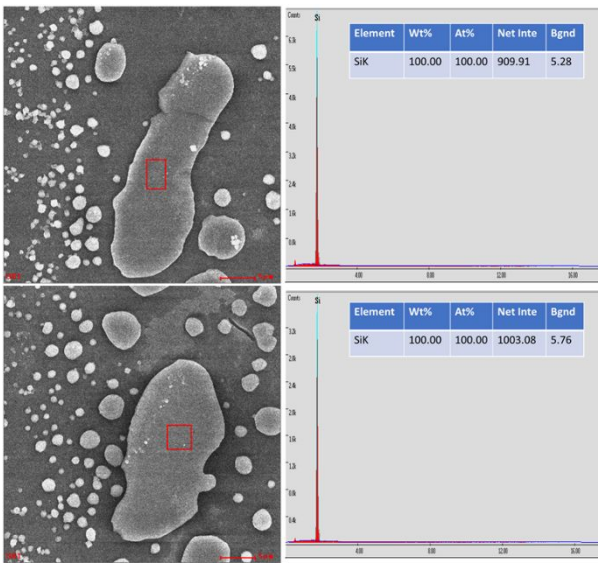

Fig. S7. EDX analysis of representative sintered Si islands.

In order to examine the elemental composition of crystallized Si islands, EDX analysis were conducted on randomly selected islands. Tiny peaks for oxygen were observed, however, the software was not able to identify such small percentage, giving a 100% of Si. Thus, it was concluded that no obvious impurity was detected.

Transfer method

We developed a transfer printing method to print the as-fabricated single-crystal islands onto flexible substrates for potential application of flexible electronic component. The detailed procedure is described below: (i) First, the Si pattern (on 2 μm thermal dioxide) was etched using 5% HF to make under-cut. The etching time can be adjusted accordingly for different patterns. (ii) Then, the sample with under-cut was cleaned with sufficient DI water and dried with nitrogen gas flow. Subsequently, the sample was dried in Ar at 350 ˚C for 30 min (allowing detachment of Polyvinyl alcohol (PVA) from SiO_2/Si during peeling off). (iii) 10 wt% PVA solution was then spin-coated using speed of 500 rpm on the sample to be transferred, followed with 110˚C baking for 3 min. (iv) Then flexible substrate (polyimide) can be used as receiving substrate on the top

PVA film. (v) Then the Si sample covered with PVA film and supported with flexible substrate can be peeled off from the edge.

Details about the heat transfer simulation

To understand the influence of quartz confinement on the heat reservation, and associated cooling rate, a simple heat conduction finite element analysis (FEA) model was developed in COMSOL to predict the temperature history. The printed Si was assumed to have a linewidth of 50 μm, length of 600 μm and thickness of 800 nm. The wafer and quartz were assumed to be 600 μm×600 μm×200 μm. For the wafer with oxide, 2 μm thermal oxide was used to replace the top 2 μm of the wafer. The dimensions and boundary conditions are illustrated in Figure S8.

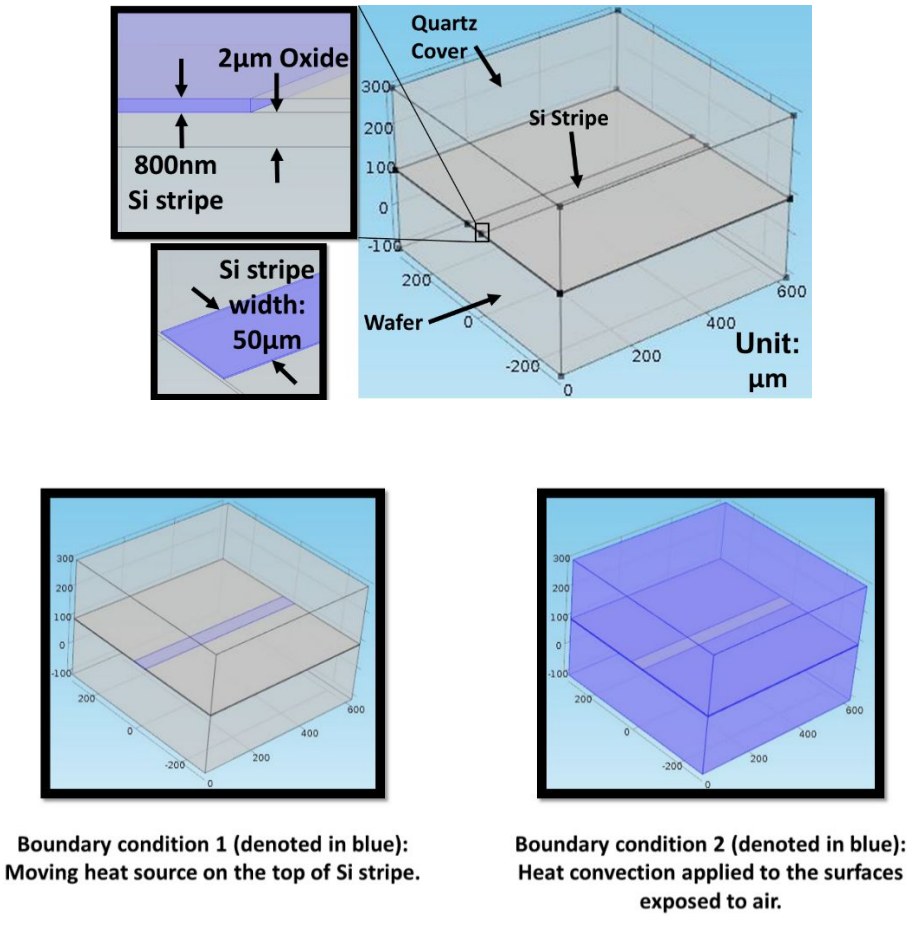

Fig. S8. Simulation domain dimensions and boundary conditions.

All the property values are tabulated in Table 1-3. The parameters of Si line were assumed to be 50% of corresponding crystalline wafer based on the assumption that the nanoparticle packing density is ~50%.

Table 1. Thermal properties of the materials used for the numerical modeling.

	Si line	Crystalline wafer	Thermal oxide
Density (kg/m^3)	1160	2320	2468
Specific heat(J/kg·K)	50% of crystalline wafer	$846+1.18\times10^{-1}T-1.55\times10^{7}/T^2$	See Table 2
Thermal conductivity (W/m·K)	50% of crystalline wafer	See Table 3	2.1

Table 2. Thermal oxide specific heat.

Temperature (K)	Specific heat (J/kg·K)
300	746.3
400	887.83
500	994.67
600	1084
750	1201
900	1143.67
1050	1152
1150	1173.83
1300	1186.167
1450	1206.083
1550	1219.75
1650	1233.75
1700	1298.5
1750	1298.5
1850	1298.5
1900	1298.5

Table 3. Thermal conductivity of crystalline Si.

Temperature (K)	Thermal conductivity (W/m·K)
300	325

400	105
500	84.5
600	64
750	48
900	37
1050	29.75
1150	27.25
1300	25
1450	23.5
1550	22.5
1650	22
1700	21.4
1750	21
1850	21
1900	21

A Gaussian laser beam [Yan2017] was adopted and defined as

$$\mathrm{I(x,y)} = \frac{\alpha P(1-\beta)}{\frac{1}{2}\pi r^2} \mathrm{e}^{-2[(x-X_t)^2 + (y-Y_{center})^2]/r^2}$$

where α is the absorption coefficient (assume 0.10 [Said-Bacar2011]), β is the reflection (assume 0.4 [Said-Bacar2011]), P is the laser power, $2r$ is the beam diameter (80 μm), X_t is the beam location along length direction at time t, Y_{center} is a constant (half of the width in y direction). The temperature dependent thermal conductivity, specific heat for silicon are from Ref. [Said-Bacar2011]. The fused silica properties were listed in the below table. The convection coefficient between substrate and air is set to be a reasonable constant value of 5 W/(m^{2}K) for all materials.

Table 4. Properties of fused quartz.

Properties	**Value**
Density	2.21×10^3 kg/m^3
Refractive index	1.5
Thermal Conductivity	1.4 W/mK

Heat capacity at constant pressure	730J/(kgK)

Crystallization model

To predict for single crystal formation in domain in various sizes, we employed a phenomenological model developed previously [Pan2015]. The heterogeneous nucleation and crystal growth were modeled using a simple two-sphere model [Cooper2008, Fletcher1958], as shown in Fig. S9, with the overlapped section representing the nucleus/crystal structure. The temperature evolution of the droplet (with the presence of crystal growth) is calculated by the energy balance equation,

$$\frac{4\pi R^3 C_v}{3v}\frac{dT_P}{dt} = \frac{\Delta H}{v}\frac{dV_S}{dt} - \frac{dE_{surface}}{dt} - (T_P - T_0)GA \qquad (1)$$

Where, T_P is droplet temperature, T_0 is surrounding temperature, C_v is the specific heat per atom, v is the atomic volume (C_v and v are assumed to be equal between liquid and solid phases), R is the radius of the droplet (or domain size), V_s is the nucleus/crystal volume, ΔH is the latent heat of melting per atom, $E_{surface}$ is the excess surface energy due to the presence of the nucleus/crystal. The first two terms on right side of Equ.1 describe the temperature change due to crystal growth, which will be zero before the detection of first nucleus.

During each Δt, it is checked if a nucleus is formed. We consider the temperature as being invariant during sufficiently small timestep Δt, and compute P^{NUC} using the Poisson equation [Leonard2001] as:

$$P^{NUC} \cong 1 - Exp(-4\pi R^2 \cdot I \cdot \Delta t) \qquad (2)$$

The value P^{NUC} can range from zero to unity, and it physically corresponds to the probability of nucleation events during the evaluated timestep. A fresh random number will be generated during each timestep and compared with P^{NUC}. If the *random number* is found to be less than P^{NUC} then the nucleation occurs. The surface nucleation rate I in Equ.3 is:

$$I = I_0 \exp\left(\frac{-\Delta F^*_{het}}{k_B T}\right) \tag{3}$$

where I_0 is the pre-factor $1\times10^{29}\mathrm{m}^{-2}$, taken from reference [Fletcher1958]. The nucleation ΔF^*_{het}, following the reference [Cooper2008], is written as,

$$\Delta F^*_{het} = \frac{8}{\Delta\mu^2}\pi\gamma_{ls}^3 v^2\left\{\frac{4}{3}[-f(\theta+\phi)+(R/r^*)^3 f(\phi)]+[1-\cos(\theta+\phi)]-\cos\theta(1-\cos\phi)(R/r^*)^2]\right\} \tag{4}$$

where θ is the contact angle between the nucleus and the droplet surface, $\cos\theta=(\gamma_{lw}-\gamma_{sw})/\gamma_{ls}$, Φ is defined in Fig.S9 [Pan2015], $\Delta\mu = -\Delta H \ln\frac{T}{T_{eq}}$ is the free energy different between the solid and liquid phase, r^* is the critical nucleus size $2\gamma_{ls}v/\Delta\mu$, γ_{lw}, γ_{sw} and γ_{ls} is the interfacial energy between the SiO_2 wall and liquid Si phase, SiO_2 wall and Si crystal/nucleus, and between Si liquid and crystal/nucleus, respectively.

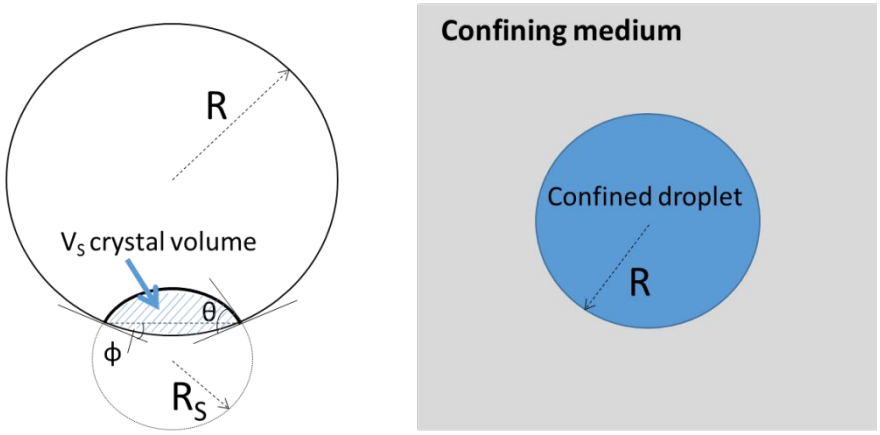

Fig. S9. Modeling liquid crystallization in confined domains.

Once the first nucleation occurs, the radius of nucleus/crystal R_S is set to be r^*, which will be updated by $R_S(t+\Delta t) = R_S(t) + V_C \Delta t$, where V_C is crystallization velocity. The nucleus/crystal volume V_S can be calculated as [Cooper2008, Pan2015],

$$V_S = \frac{4}{3}\pi R_S{}^3 [f(\theta+\phi) - (R/R_S)^3 f(\phi)] \quad (5)$$

and the excess surface energy due to the existence of crystal is [Cooper2008, Pan2015],

$$E_{surf} = 2[1-\cos(\theta+\phi)]\pi R_S{}^2 \gamma_{ls} + 2(1-\cos\phi)\pi R^2(\gamma_{sw} - \gamma_{lw}) \quad (6)$$

In each time step, both V_S and E_{surf} will be re-calculated with updated value of R_S, then dV_s/dt and dE_{surf}/dt will be calculated and used in Equ. (1) for temperature updates. The above equations (1-6) will be iterated until a second nucleation event occurs or crystal fraction $V_S/(4\pi R^3/3)$ reaches 70%. If no second nucleus was detected, the simulation run was declared as a "single-crystal" event, and otherwise a "poly-crystal" one.

The parameters used in modeling are summarized in the following table. Note that values for ΔH, T, and γ_{ls} are taken from molecular dynamics of liquid Si nucleation using Tersoff potential [Li2009] and value for γ_{sw}-γ_{lw} is taken from Molecular Dynamics simulation of liquid Si nucleation on SiO_2 surface using Tersoff potential [Shou2016].

Table 5. Parameters for the phenomenological model

Specific heat (eV/K/atom)	Atomic volume (nm^3/atom)	Latent heat (eV/atom)	Bulk melting point (K)	Atomic mass (kg)	Time step (s)	interfacial surface energy (J/m^2)	
C_v	v	ΔH	T_{eq}	m	Δt	γ_{sw}- γ_{lw}	γ_{ls}
2.06e-4	0.0203	0.407	2540	4.66e-26	1e-10	0.2	0.29

To simulate laser heating experiments, the laser profile and substrate heat loss need to be considered. We consider a simple case with a particle embedded in infinite medium. It is assumed that the confining medium is optically transparent and laser irradiation only heats the particle/droplet. To compute particle temperature, laser irradiation is introduced to Equ.1 as in the following, where T_0 is the medium temperature at the particle/medium interface and G is the interfacial thermal conductance,

$$\frac{4\pi R^3 C_v}{3v}\frac{dT_P}{dt} = \frac{\Delta H}{v}\frac{dV_S}{dt} - \frac{dE_{surface}}{dt} - (T_P - T_0)GA + \pi R^2 J(t) \tag{7}$$

The laser pulse exhibits a Gaussian temporal profile whose intensity can be modeled as,

$$J(t) = J_0 \exp\left(-\left(\frac{t - t_c}{w}\right)^2\right) \tag{8}$$

where J_0 is the peak laser intensity, w is the laser pulse width and t_c is the time when laser intensity reaches its maximum. The confining medium temperatures (including T_0) will be calculated based on a heat conduction model considering only radial thermal gradient,

$$\rho C_p \frac{\partial T_{sub}}{\partial t} = \frac{1}{r^2}\frac{\partial}{\partial r}\left(kr^2 \frac{\partial T_{sub}}{\partial r}\right) \tag{9}$$

wherein thermal properties of Silicon (C_p = 700 kJ/kg·K, ρ = 2203kg/m^3 and k = 148W/m·K) have been used for the confining medium. The thermal conductance between the particle and confining medium is assumed to be 1e7 W/m^{2}K which is used to represent a thin layer of oxide ~100nm thick. The above equations (Equ. 1-9) were integrated numerically in spatial and temporal domains using explicit schemes to update substrate temperature and particle temperature at each time step.

References

[1]. Yan, Lei, et al. "Simulation of Cooling Rate Effects on Ti-48Al-2Cr-2Nb Crack Formation in Direct Laser Deposition." Jom 69.3 (2017): 586-591.
[2]. Said-Bacar, Z., et al. "Modeling of CW Laser Diode Irradiation of Amorphous Silicon Films." Applied Surface Science 257.12 (2011): 5127-5131.
[3]. Hartnett, Chris A., et al. "Instability of Nano- and Microscale Liquid Metal Filaments: Transition from Single Droplet Collapse to Multidroplet Breakup." Langmuir 31.50 (2015): 13609-13617.
[4]. Ubal, Sebastián, et al. "The Influence of Inertia and Contact Angle on the Instability of Partially Wetting Liquid Strips: A Numerical Analysis Study." Physics of Fluids 26.3 (2014): 032106.
[5]. Zhao, Junlei, et al. "Crystallization of Silicon Nanoclusters with Inert Gas Temperature Control." Physical Review B 91.3 (2015): 035419.
[6]. Stillinger, Frank H., and Thomas A. Weber. "Computer Simulation of Local Order in Condensed Phases of Silicon." Physical review B 31.8 (1985): 5262.
[7]. Pan, Heng, and Wan Shou. "Single Crystal Formation in Micro/Nano-Confined Domains by Melt-Mediated Crystallization without Seeds." Journal of Physics D: Applied Physics 48.22 (2015): 225302.
[8]. Cooper, Sharon J., Catherine E. Nicholson, and Jian Liu. "A Simple Classical Model for Predicting Onset Crystallization Temperatures on Curved Substrates and Its Implications for Phase Transitions in Confined Volumes." The Journal of chemical physics 129.12 (2008): 124715.
[9]. Fletcher, N. H. J. "Size Effect in Heterogeneous Nucleation." The Journal of chemical physics 29.3 (1958): 572-576.
[10]. Leonard, J. P., and James S. Im. "Stochastic Modeling of Solid Nucleation in Supercooled Liquids." Applied Physics Letters 78.22 (2001): 3454-3456.
[11]. Li, Tianshu, Davide Donadio, and Giulia Galli. "Nucleation of Tetrahedral Solids: A Molecular Dynamics Study of Supercooled Liquid Silicon." The Journal of chemical physics 131.22 (2009): 224519.
[12]. Shou, Wan, and Heng Pan. "Silicon-Wall Interfacial Free Energy via Thermodynamics Integration." The Journal of chemical physics 145.18 (2016): 184702.